The Influence of High-Frequency Tidal Processes on the Shoreward Transmission of Low-Frequency Open-Ocean Signals

WENQIANG LIN,[a] HONGYANG LIN,[b] JIANYU HU,[b] AND LINGFENG HUANG[a]

[a] *State Key Laboratory of Marine Environmental Science, College of the Environment and Ecology, Xiamen University, Xiamen, China*
[b] *State Key Laboratory of Marine Environmental Science, College of Ocean and Earth Sciences, Xiamen University, Xiamen, China*

(Manuscript received 17 May 2024, in final form 3 July 2025, accepted 18 July 2025)

ABSTRACT: The on-shelf penetration of low-frequency open-ocean signals makes a significant contribution to the variability of coastal sea level. However, owing to the complicated coupling, the high-frequency tidal effects on the shoreward penetration of the low-frequency signals are generally overlooked. This study revisits the classic β-plane arrested topographic wave model aiming to more explicitly reveal the role of tides in modulating the open-ocean sea level transmission over the continental shelf. By inferring and comparing different forms of the vorticity equation, we reexpress the bottom friction coefficient (BFC) as $r = f\delta_B = \kappa\sqrt{\tau_b/\rho}$ based on a linear eddy-viscosity parameterization, thereby relating BFC to the thickness of the bottom boundary layer δ_B and further to the bed shear stress (BSS) τ_b (f being the Coriolis parameter, κ being a constant, and ρ is the seawater density). This provides a novel perspective to examine tidal effects on the across-shelf transmission by estimating enhanced BSS induced with the addition of tidal currents. Using appropriate parameterizations to estimate BSS, we apply the calculations to the western North Atlantic. It is shown that BFC exhibits an abrupt increase between 28° and 35°N by including tidal currents, which enhances the on-shelf penetration of open-ocean signals, especially in the downstream vicinity of 31°N. Moreover, modeling experiments indicate that this enhancement is more evident for shorter-wavelength signals. Such a pronounced coastal response is clearly manifested in tide gauge measurements along the east coast of North America. We also discuss the impact of tidal current rotation on the ocean-to-coast transmission for a constant eddy-viscosity scenario.

SIGNIFICANCE STATEMENT: Large-scale, low-frequency sea level signals from the deep ocean propagate across the continental slope and shelf to the coast, significantly altering coastal sea level variations. However, the effect of high-frequency tides on the shoreward transmission of open-ocean signals is largely overlooked. We rederive a new expression for the bottom friction coefficient, incorporating the seabed shear stress, allowing us to more explicitly examine the tidal effects. The modeling solutions show that the tidal currents aid the cross-shore transmission particularly near 31°N, and the coast is more likely to experience shorter-wavelength signals from the deep ocean due to the addition of tidal currents. Such an enhanced shoreward transmission near 31°N is clearly observed as a pronounced coastal response from the tide gauge measurements along the east coast of North America.

KEYWORDS: Continental shelf/slope; Ocean dynamics; Sea level; Tides

1. Introduction

Low-frequency, deep-ocean sea level signals, driven by large-scale wind stress over the ocean basin interior, propagate westward in the form of barotropic and baroclinic Rossby waves (e.g., Qiu 2002, 2003), then penetrate shoreward across the continental slope and shelf, ultimately reaching the coast (Lin et al. 2022). It is traditionally recognized that the coast can only "feel" large-scale (typically thousands of kilometers) signals from the deep ocean owing to an insulating effect produced by the presence of the inclined continental shelf (Huthnance 2004; Wise et al. 2018), although a recent study demonstrates that open-ocean signals with an along-shelf length scale comparable to the shelf width can also significantly affect the coast (Wu 2023). This open-ocean-induced coastal sea level setup serves as an important baseline with the potential to amplify short-term sea level fluctuations caused by extreme events such as storm surges (Boumis et al. 2023), a typical type of natural disaster that dramatically threatens the socioeconomic development of coastal areas (Ji et al. 2019). Therefore, the accuracy of projections of coastal flood risk depends on the capability to capture coastal sea level variability at both short- and long-time scales.

Regarding factors that influence the shoreward transmission of deep-ocean sea level signals, previous studies have examined the effects of stratification (Brink 2006), friction (Wise et al. 2018; Wu 2021), bottom topography (Higginson et al. 2015; Minobe et al. 2017), and the spatial scale of open-ocean forcing (Lin et al. 2022) but generally overlooked the effect of high-frequency processes (e.g., tides). This omission is due in part to the relatively unimportant effect of time dependence in the long-wave limit for periods longer than a few days (Csanady 1978; Middleton and Thompson 1985; Hughes et al. 2019) and also to the complexity in representing dynamical couplings across a wide range of time scales (Huthnance 2004). While previous attempts have been made to consider the time variation of offshore signals, they mostly emphasized subinertial variability (i.e., with time scales longer than several days or months) (Marshall and Johnson 2013; Wu 2023).

Corresponding author: Hongyang Lin, hylin@xmu.edu.cn

Publisher's Note: This article was revised on 11 December 2025 with a corrected version of Fig. 1.

DOI: 10.1175/JPO-D-24-0082.1

Huthnance (2004) and Wu (2023) mentioned that tides, as examples of barotropic gravity waves, can aid cross-shelf transmission of interior sea level; nevertheless, this demonstration is largely a general conclusion from scale analysis. Considering the depth-integrated alongshore momentum balance, $\partial v/\partial t + rv/h = F_y/\rho h$ (where v is the alongshore component of flow, t is the time, r is a linear friction coefficient, h is the water depth for the coastal ocean, F_y is the alongshore wind stress, and ρ is the seawater density), the influence of flows with an oscillating frequency ($\partial/\partial t \to \omega$) is equivalent to that of the drag r/h (Hughes et al. 2019). It implies that high-frequency processes are expected to play a similar role to large friction, namely, aiding cross-shelf transmission of open-ocean signals. For the high-frequency processes mentioned above, we focus specifically on tides in this study.

The influence of tides on the shoreward propagation of deep-ocean signals could manifest through several mechanisms. One typical mechanism is tidal mixing, which can be represented in different ways. Specifically, tidal mixing can manifest as tidal mixing fronts (or tidal downward stirring of the surface heat; Simpson et al. 1990; Hill et al. 2008) in the interior layer, or as turbulence caused by tide-induced drag on the seabed (Garrett and Kunze 2007; Suanda et al. 2017). The former is useful for understanding the role of ocean stratification in altering the sea level responses to oceanic forcing particularly on the continental slope (e.g., Brink 1991; Huthnance 2001). The latter is useful for explaining phenomena like the bottom boundary layer (BBL). Here, our emphasis will be on the BBL dynamics, which are closely linked to bottom friction (see details later) that strongly affects the penetration of open-ocean signals across the shelf. For simplicity, we assume in this study that the tidal currents are relatively strong, and hence the water column on the shelf is vertically well mixed by tidal stirring/mixing (Simpson and Hunter 1974); we thus neglect the tide-induced stratification effect on the shelf response to open-ocean processes. Indeed, the shelf response is largely barotropic, as pointed out by Chapman and Brink (1987).

Therefore, we aim to investigate the effect of BBL dynamics, induced by tidal current oscillation, on the ocean-to-coast transmission, and thereby to build a connection between high-frequency processes (tides) and the low-frequency shoreward transmission. The manuscript is structured as follows. Section 2 presents a new model and its comparison with the classic model of a β-plane arrested topographic wave (ATW), which is frequently used to describe the transmission of deep-ocean signals. In section 3, we design idealized numerical experiments to examine the tidal effects with the aid of the reformulated β-plane ATW model, and the comparisons between model results and tide gauge observations are presented in section 4. The results are summarized and discussed in section 5.

2. Recasting the β-plane ATW model

a. Classic formulation of the β-plane ATW model

Csanady (1978) applied a steady f-plane barotropic model to identify that the sea level response observed over the shelf is produced by an alongshore sea level gradient imposed at the edge of the shelf by the dynamics of a deep-ocean current; this model was termed the f-plane ATW model. For applications where the alongshore scale of the forcing is large, Middleton and Thompson (1985) later generalized the ATW model by allowing f to vary. Wise et al. (2018) and Wu (2021) further developed the linear β-plane ATW model to describe the relationship between coastal sea level and deep-ocean dynamics. This β-plane model can explain the observational fact that the interior sea level can penetrate to the coast while attenuating in magnitude and displacing equatorward in position (e.g., Higginson et al. 2015; Lin et al. 2021). Without loss of generality, here we will use this classic β-plane ATW model to describe the transmission of deep-ocean sea level and then to examine the tidal effects.

For a β plane, steady-state, linearized, and barotropic shelf with the y axis coinciding with the coast and the water depth changing offshore only, the governing equations are

$$-fv = -g\frac{\partial \eta}{\partial x}, \tag{1a}$$

$$fu = -g\frac{\partial \eta}{\partial y} + \frac{F_y}{h} - \frac{rv}{h}, \tag{1b}$$

$$\frac{\partial (uh)}{\partial x} + \frac{\partial (vh)}{\partial y} = 0, \tag{1c}$$

where u, v, η, $h = h(x)$, and g are cross-shore velocity, alongshore velocity, sea level, water depth, and gravitational acceleration, respectively. To simplify the calculation, we assume the cross-shelf dynamics are in geostrophic balance (i.e., $|ru/h| \ll |fv|$ and $|F_x/h| \ll |fv|$). Namely, Eq. (1) is valid only when the along-shelf scale is much larger than the shelf width. The $f = f_0 + \beta y$ is the Coriolis parameter, $\mathbf{F} = (F_x, F_y)$ is the kinematic wind stress, and r is the bottom friction coefficient (BFC). For simplicity, here we only consider the western boundary oriented in the meridional direction. Taking the curl of Eq. (1), the β-plane ATW model can be represented in several different forms that are all mathematically equivalent (essentially a vorticity equation):

$$r\eta_{xx} + fh_x\eta_y + \beta h\eta_x = \mathbf{S}_1, \tag{2}$$

$$-\nabla\cdot(\gamma\nabla\eta) + \mathbf{U}\cdot\nabla\eta = \mathbf{S}_2, \tag{3}$$

$$\beta v = \frac{\partial}{\partial x}\left(\frac{F_y}{h} - \frac{rv}{h}\right) + \frac{f}{h}h_x u, \tag{4}$$

where subscripts denote differentiation, ∇ is the horizontal differential operator, $\gamma = gr/f^2$ can be seen as the diffusion coefficient, $\mathbf{U} = (U, V) = \nabla(gh/f) \times \mathbf{k}$ can be seen as the advection velocity which is perpendicular to the gradient of gh/f (i.e., sea level η would be "advected" tangentially to the contours of gh/f); $\mathbf{S}_1 = f^2\nabla \times [\mathbf{F}/(f\rho g)]$ and $\mathbf{S}_2 = -\nabla \times [\mathbf{F}/(f\rho)]$ indicate the curl of wind stress.

In Eq. (2), the first term is proportional to the relative vorticity, the second term is the topographic term which describes the vortex stretching/squeezing, and the third term is the planetary vorticity due to the β effect. This indicates that the imported vorticity, induced by, for example, a negative wind stress curl, is associated with a decrease in the relative/planetary

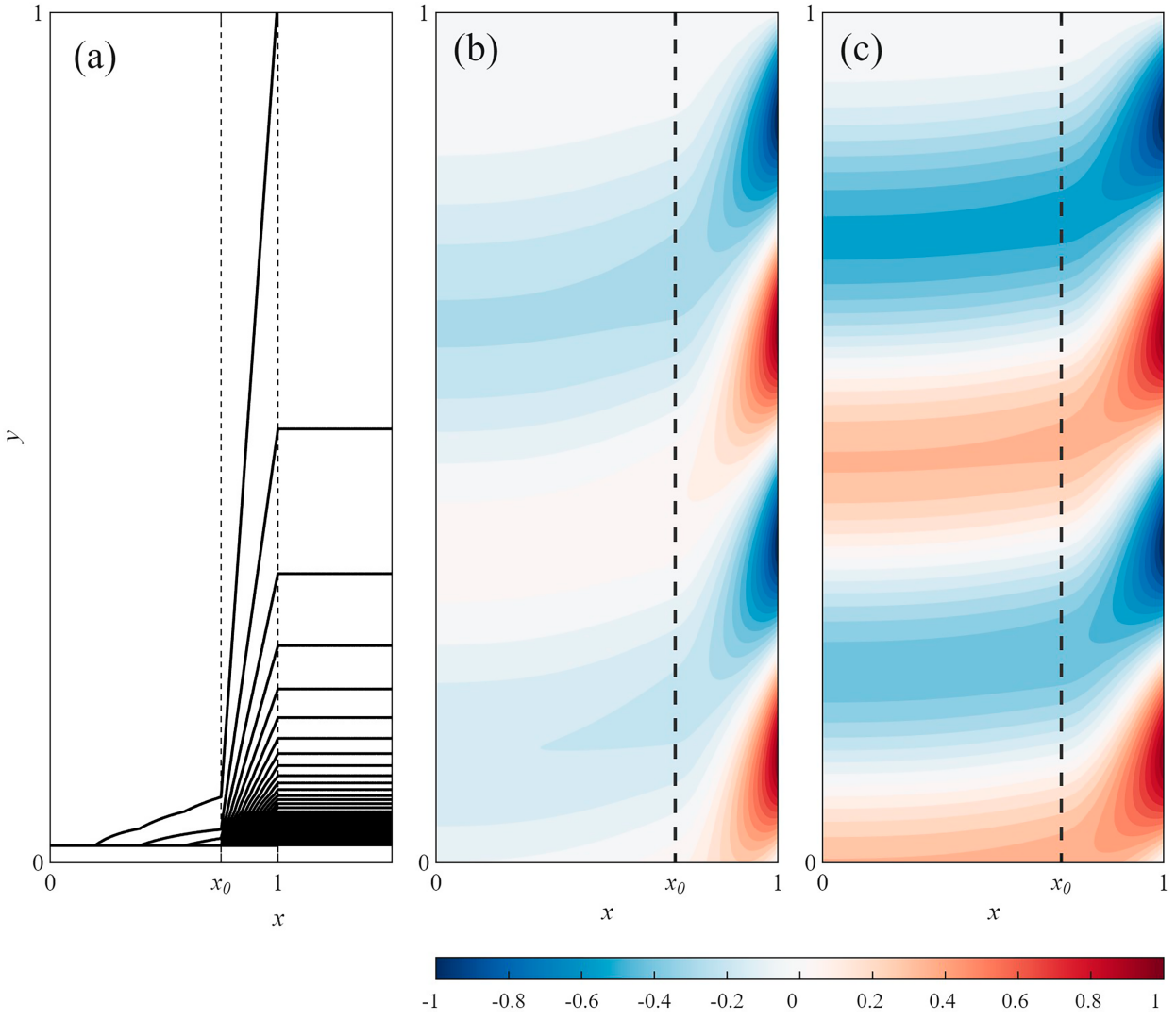

FIG. 1. (a) Potential vorticity contours of gh/f. Vertical dotted lines denote the shelf break at $x = x_0$ and the slope break at $x = 1$. Nondimensional across- and alongshore coordinates are given by x and y, respectively. Western boundary sea level contours for (b) lower-friction solutions and (c) higher-friction solutions. The sea level is normalized by the amplitude of open-ocean signals. The equator is at $y = 0$, and the northern boundary is at $y = 1$.

vorticity, or a vortex stretching, so as to conserve potential vorticity. Besides, with prescribed boundary conditions, we can straightforwardly characterize the transmission of interior sea level by numerically solving Eq. (2), which is a single equation for sea level η. With regard to Eq. (3), the first term is the diffusion term, and $\mathbf{U}$ in the second term is simply a westward flow at the long Rossby wave speed (planetary or topographic Rossby wave). This implies that a rise in sea level caused by the source term S_1 or S_2 is advected along the potential vorticity contours of gh/f (Fig. 1a), while it can also be diffused across the gh/f contours by the action of bottom friction, which allows open-ocean sea level signals to penetrate toward the coast (Figs. 1b,c). As friction increases, the penetration of open-ocean signals increases accompanied by reduced equatorward displacement (cf. Figs. 1b,c). In Eq. (4), the first term is the poleward meridional transport, the second term is the stress curl at the top and bottom of the ocean, and the last term indicates the zonal transport (i.e., cross-shore transport). Equation (4) reduces to the Stommel model (Stommel 1948) in the flat-bottom case (i.e., ignoring the last term). This means that a poleward-flowing current in the flat-bottom western boundary must be frictional, but in the case with a sloping shelf at the western boundary, the poleward-flowing current can also move offshore so as to preserve its potential vorticity.

Although each form of the β-plane ATW model in Eqs. (2)–(4) has its own strength in physical interpretation, these forms do not explicitly illustrate the roles of high-frequency processes (i.e., tides). Possible tidal effects may be contained in Eq. (4) by affecting the linear friction for bottom stress (ru): larger friction favors shoreward penetration of offshore signals with less equatorward displacement (e.g., Wise et al. 2018). However, the role of bottom friction is generally examined by

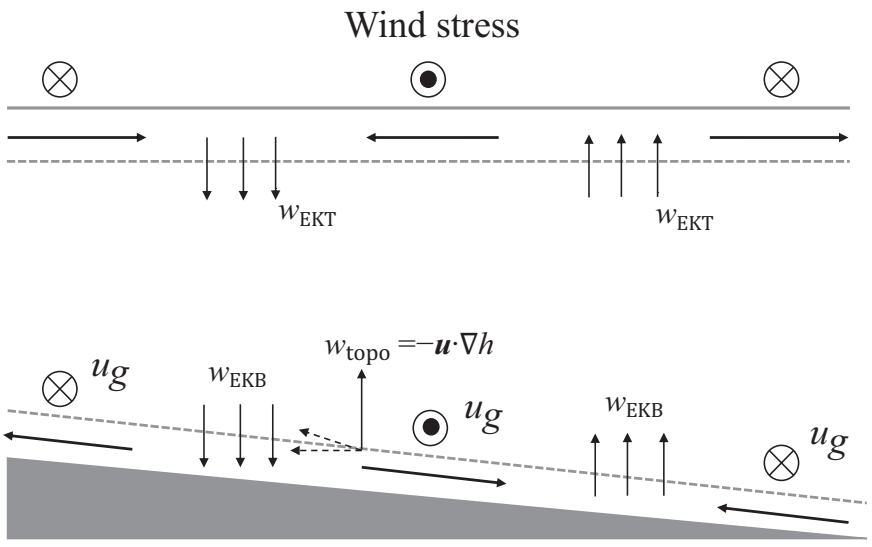

FIG. 2. Schematic of the three-layer coastal ocean with a sloping topography. The top Ekman layer is mainly forced by an imposed wind stress, whereas the bottom Ekman layer results from the interaction of geostrophic currents (u_g) in the interior layer with bottom topography. The w_{EKT} and w_{EKB} mean the vertical Ekman pumping velocities resulting from the given wind stress curl and the interior geostrophic flow, respectively. The w_{topo} means the vertical velocity induced by barotropic currents flowing over the bottom topography.

prescribing different values of the BFC r in previous studies (e.g., Lin et al. 2022), which does not specifically isolate the tidal effect. Hence, we will derive an alternative expression of r, which explicitly includes tidal dynamics, to obtain a modified formulation of the β-plane ATW model.

b. *A modified formulation of the β-plane ATW model*

Rather than assuming a barotropic single layer, we consider that the coastal ocean with a sloping bottom can be divided into three layers: the interior geostrophic layer, the upper Ekman layer, and the bottom Ekman layer (Fig. 2). The governing equations for the flow in the homogeneous midlayer are therefore:

$$-fv = -g\frac{\partial \eta}{\partial x}, \tag{5a}$$

$$fu = -g\frac{\partial \eta}{\partial y}, \tag{5b}$$

$$\frac{\partial u}{\partial x} + \frac{\partial v}{\partial y} + \frac{\partial w}{\partial z} = 0. \tag{5c}$$

Cross differentiating Eqs. (5a) and (5b) gives

$$v\frac{\partial f}{\partial y} + f\left(\frac{\partial u}{\partial x} + \frac{\partial v}{\partial y}\right) = 0. \tag{6}$$

Using the continuity Eq. (5c) $\partial w/\partial z = -(\partial u/\partial x + \partial v/\partial y)$, we then obtain

$$\beta v = f\frac{\partial w}{\partial z}, \tag{7}$$

which is the linear geostrophic vorticity balance, meaning that water column stretching in the presence of rotation is balanced by a change in latitude. If we restrict the vertical velocity w to be induced only by surface Ekman pumping and neglect that induced by the interaction with bottom topography, the linear geostrophic vorticity balance reduces to the Sverdrup balance, $\beta v = \mathrm{curl}_z\mathbf{F}$.

At the interior edge of the top and bottom boundary layers, the stresses approach zero, but the vertical velocities are not zero. At the base of the surface Ekman layer, the vertical velocity is

$$w_{EKT} = \mathrm{curl}_z(\mathbf{F}/f_0). \tag{8}$$

Similarly, at the top of the bottom Ekman layer, the vertical velocity is (Cushman-Roisin 1994)

$$w_B = w_{EKB} + w_{topo}, \tag{9}$$

where w_{EKB} is the bottom Ekman pumping velocity and $w_{topo} = -\mathbf{u}\cdot\nabla h$ is the vertical velocity induced by the geostrophic flow $\mathbf{u}$ flowing over the bottom topography. Integrating over the ocean interior between the two Ekman layers, Eq. (7) becomes

$$\begin{aligned}\beta h v &= f(w_{EKT} - w_B) = f(w_{EKT} - w_{EKB} - w_{topo})\\ &= f\mathrm{curl}_z(\mathbf{F}/f_0) - fw_{EKB} + f\mathbf{u}\cdot\nabla h.\end{aligned} \tag{10}$$

Equation (10) is an alternative form of Eq. (4), except with the bottom friction term replaced by the bottom Ekman pumping w_{EKB}, which, as will be shown shortly, more explicitly illustrates the effect of the tidal dynamics. Strictly speaking, h of Eq. (10) is the vertical integration distance between the bottom of the surface Ekman layer and the top of the bottom Ekman layer. Here, we essentially assume that the two Ekman layers are much thinner than the water depth. In fact,

we can also obtain Eq. (10) by integrating over the whole water depth, but in that case the vertical velocities vanish at the boundaries, while the frictional stresses do not.

When the eddy viscosity is constant, the traditional bottom Ekman pumping is expressed as (Pedlosky 1987)

$$w_{\mathrm{EKB}} = \sqrt{\frac{2A_v}{f}}\left(\frac{\partial v_g}{\partial x} - \frac{\partial u_g}{\partial y}\right) = \delta_B \zeta, \tag{11a}$$

$$\delta_B = \sqrt{\frac{2A_v}{f}}, \tag{11b}$$

where A_v is the eddy viscosity, u_g and v_g are the zonal and meridional components of the geostrophic flow aloft, δ_B is the thickness of the bottom Ekman layer (in fact, the expression of δ_B also holds for the linear eddy-viscosity model), and $\zeta = \partial v_g/\partial x - \partial u_g/\partial y = g/f(\partial^2\eta/\partial x^2 + \partial^2\eta/\partial y^2)$ is the relative vorticity of the geostrophic flow. Substituting Eq. (11a) into Eq. (10), we obtain

$$\beta h v = f\mathrm{curl}_z(\mathbf{F}/f_0) - f\delta_B\zeta + f\mathbf{u}\cdot\nabla h. \tag{12}$$

We can see that Eq. (12) is mathematically equivalent to Eq. (4) if the cross-shore wind stress and alongshore variation of topography are neglected, and also the BFC is reexpressed as (Vallis 2017)

$$r = f\delta_B, \tag{13}$$

which provides an alternative perspective for us to investigate tidal effects on the shoreward transmission of open-ocean signals by examining variations of the BBL on the continental shelf/slope.

c. *A further extension of r*

In the BBL (e.g., bottom Ekman layer), δ_B is defined by the velocity or turbulence profiles, which depend strongly on the nature of the free-streamflow above the BBL. There are various types of free-streamflows in the ocean (e.g., forced by winds, tides, or buoyancy); they can act separately or in conjunction with each other on the BBL. One key point of this study is to examine how the addition of tidal flows to the mean flow modifies the dynamics of the BBL (e.g., the variations of BBL thickness). Previous studies on BBL dynamics related to tides have focused on, for example, the distributions of energy spectra, Reynolds stresses, or turbulence dissipation in the BBL (e.g., Soulsby 1983; Gross and Nowell 1985; Luznik et al. 2007). Here, we assess the thickening or thinning of the BBL thickness (δ_B) due to the superimposed tidal currents by calculating the seabed shear stress, which measures the rate of momentum transfer and varies with the eddy viscosity.

The frictional stress can be modeled with an eddy viscosity as (e.g., Prandle 1982)

$$\tau = \rho A_v \frac{\partial \mathbf{U}}{\partial z}, \tag{14}$$

where ρ is the seawater density, z is the height above the seabed, and $\mathbf{U}$ is the time-mean velocity. The eddy viscosity A_v is not a constant but is location and flow dependent. Hence, we adopt a more realistic parameterization (i.e., the law-of-the-wall parameterization; Ellison 1956):

$$A_v = \kappa u_* z, \tag{15}$$

where κ is the von Kármán constant ~0.4 (Baumert 2009) and u_* is the friction velocity. Most geophysical flows have been observed to follow the law of the wall (Schlichting and Gersten 2016). The friction velocity is defined as (e.g., Soulsby 1997)

$$u_* = \sqrt{\tau_b/\rho}, \tag{16}$$

where τ_b is the shear stress near the bottom [or bed shear stress (BSS)]. According to the linear eddy-viscosity model, the relationship between δ_B and u_* can, in fact, be derived from scale analysis of the momentum balance by assuming that the horizontal frictional stress is comparable to the Coriolis force: $fv \sim \partial/\partial z[\kappa u_* z(\partial u/\partial z)]$. A scale analysis gives $\kappa u_*/f\delta_B \sim 1$, that is

$$\delta_B = \kappa\frac{u_*}{f} = \kappa\frac{\sqrt{\tau_b/\rho}}{f}. \tag{17}$$

Previous studies have generally used this scale to characterize the BBL thickness (e.g., Saylor 1994; Perlin et al. 2007). We can see that when relaxing the assumption of a constant eddy viscosity, the expression for δ_B in Eq. (17) is not qualitatively different from that in Eq. (11b). Using Eq. (17) in Eq. (13), we obtain

$$r = f\delta_B = \kappa\sqrt{\tau_b/\rho}. \tag{18}$$

The BFC r is thus related to the BSS τ_b. Equation (18) is the fundamental basis for our further analysis in this study. It differs from the traditional practice of using a spatially uniform r in the classic β-plane ATW model and also suggests that the inhomogeneity of r is closely related to the distribution of τ_b. Furthermore, the redefined formula [(18)] now allows us to consider the tidal effects as long as the total τ_b can be properly estimated.

The usual quadratic law is used for BSS (Soulsby 1983; Lee et al. 2000):

$$\tau_b = \rho C_D\left(\sqrt{u_b^2 + v_b^2}\right)^2, \tag{19}$$

where C_D is the bottom drag coefficient ($C_D = 0.0025$) and u_b and v_b are the zonal and meridional components of velocity at the bottom, respectively. Note that u_b and v_b do not include tidal velocities in this formulation.

Enhanced BSS due to the addition of tidal current is incorporated in this parameterization as a linear-type bottom friction as described by Hunter (1975), instead of a quadratic law:

$$\tau_{bt} = \rho C_D \gamma\sqrt{u_b^2 + v_b^2}, \tag{20}$$

where γ is given by (Lee et al. 2000)

$$\gamma = 1.23\sqrt{(\overline{u_t})^2+(\overline{v_t})^2}, \tag{21}$$

where $\overline{u_t}$ and $\overline{v_t}$ represent the depth-averaged tidal velocity in the zonal and meridional directions, respectively.

Substituting Eqs. (19) and (20) into Eq. (18) yields expressions for BFC r without (r_b) and with (r_{bt}) tidal effects, respectively:

$$r_b = \kappa\sqrt{\tau_b/\rho} = \kappa\sqrt{C_D(\sqrt{u_b^2+v_b^2})^2}, \tag{22a}$$

$$r_{bt} = \kappa\sqrt{\tau_{bt}/\rho} = \kappa\sqrt{C_D\gamma\sqrt{u_b^2+v_b^2}}$$
$$= \kappa\sqrt{1.23C_D\sqrt{(\overline{u_t})^2+(\overline{v_t})^2}\sqrt{u_b^2+v_b^2}}. \tag{22b}$$

Equation (22b) explicitly introduces the additional impact of tides on modifying the BFC. It indicates that r_{bt} would be greater than r_b in the presence of strong tidal currents, which is often the case on continental shelves. Hence, the inclusion of tides indeed would enhance the penetration of sea level to the coast.

3. Tidal effects on the ocean-to-coast transmission

Based on Eqs. (19)–(21), we can estimate BSS induced by mean currents alone and by the combined mean and tidal currents. The enhanced BSS is then used to estimate BFC r via Eq. (22), which allows us to explore the tidal effects on the ocean-to-coast transmission. In this section, we examine the above processes in a realistic ocean using reanalysis and tidal datasets and also conduct numerical experiments with an idealized barotropic model to verify the findings.

a. BFC increase due to the addition of tidal flows

We select the western North Atlantic as a testbed to examine how tides modify the spatial distribution of BFC. This region is selected because of its relatively smooth coastline and the absence of large islands that might influence the shoreward transmission. According to Eqs. (19)–(21), we first need to estimate the velocities at the bottom (u_b and v_b) and depth-averaged tidal velocities ($\overline{u_t}$ and $\overline{v_t}$). The mean flow without tidal forcing is obtained from the Copernicus Marine Environment Monitoring Service (CMEMS) global reanalysis (product ID: GLOBAL_MULTIYEAR_PHY_001_030) that is gridded, monthly, and has a resolution of 0.083° × 0.083° and 50 standard levels. The zonal and meridional components of the tidal current are obtained from the TPXO8 database. Since in the western North Atlantic diurnal tidal currents (K_1) are one order of magnitude smaller than semidiurnal tidal currents (M_2) (figure not shown), we only consider the contribution of the dominant M_2 tide to BFC variations.

With the bottom velocities and tidal currents (Fig. 3), we obtain the spatial distributions of BSS induced by mean currents alone (τ_b) and by the combined mean and tidal currents (τ_{bt}) (Figs. 4a,b). The τ_b is relatively uniform in space, with a spatial mean value of ~0.023 N m^{-2} and a standard deviation of 0.024 N m^{-2} (Fig. 4a). In contrast, τ_{bt} has significant spatial variations, with a larger standard deviation of 0.038 N m^{-2} (Fig. 4b). In particular, τ_{bt} exhibits higher values between 32° and 36°N (mean value of ~0.19 N m^{-2}) compared with those south of 32°N (~0.07 N m^{-2}), corresponding to the enhanced M_2 tidal currents within this latitudinal band (see Fig. 3b). The relatively high-value feature is further evident in the zonal-mean profile of τ_{bt} (Fig. 4c) which shows a mean value of ~0.14 N m^{-2} between 28° and 35°N, approximately 7 times greater than the mean value of τ_b (0.02 N m^{-2}). This clearly demonstrates the role of tidal currents in enhancing BSS (τ_{bt}).

We can subsequently obtain the spatial distributions of BFC induced by the mean current–alone BSS (r_b) and by the total BSS (r_{bt}). Similar to τ_b, r_b is also quite spatially uniform (Fig. 4d) with a mean value of ~1.5 × 10^{-3} m s^{-1} and standard deviation of 4.8 × 10^{-4} m s^{-1}, respectively. Likewise, the r_{bt} distribution (Fig. 4e) resembles that of τ_{bt} (Fig. 4b), showing a high value of ~5.1 × 10^{-3} m s^{-1} between 32° and 36°N. The ratio of zonal-averaged r_{bt} and r_b (r_{bt}/r_b) is elevated between 28° and 35°N with a peak ratio of ~7 located near 31°N (Fig. 4f). This abrupt meridional change in r_{bt} caused by the addition of tidal currents is expected to influence the on-shelf penetration of open-ocean signals.

b. Effect of tides on the on-shelf penetration

We then conduct numerical experiments to examine the effect of meridionally varying BFC on the on-shelf penetration of offshore signals. The β-plane ATW model [Eq. (1)] is configured for a horizontal 2D rectangular domain, with a 200-km cross-shore width mimicking the shelf width of the western North Atlantic and a latitude range from 20° to 60°N. The β is set to be constant (i.e., 1.74 × 10^{-11} m^{-1} s^{-1}). Equation (2) is numerically solved with two lateral boundary conditions, i.e., (i) the no-normal-transport boundary condition at the coast and (ii) the open-ocean boundary condition. The local wind stress is set to zero since we concentrate more on the shoreward propagation of open-ocean signals. Moreover, the northern boundary condition would not affect the transmission of open-ocean signals in this linear model (figures not shown) and is thus set to zero.[1]

The impact of tidal currents on the ocean-to-coast transmission, via changing the BSS and then BFC profile, can be assessed using two metrics. First, we examine the sea level amplitude over the shelf. Figures 5a and 5b show the sea level response corresponding to the two BFC profiles shown in Fig. 5c; for the tide-excluded case (black line in Fig. 5c), the r_b profile uses the spatial mean (~1.5 × 10^{-3} m s^{-1}) of BFC in Fig. 4d; for the tide-included case, the r_{bt} profile (red line in Fig. 5c) is derived by multiplying the r_{bt}/r_b (Fig. 4f) ratio by 1.5 × 10^{-3} m s^{-1}. It is seen that without tidal effect (Fig. 5a), the coastal sea level is a

[1] Although the northern boundary condition does not affect the on-shelf transmission, it could influence specific values of the modeled η, particularly near the northern boundary; nonetheless, a sufficiently long alongshore domain can effectively minimize this effect, allowing us to focus on the model solutions in the southern region.

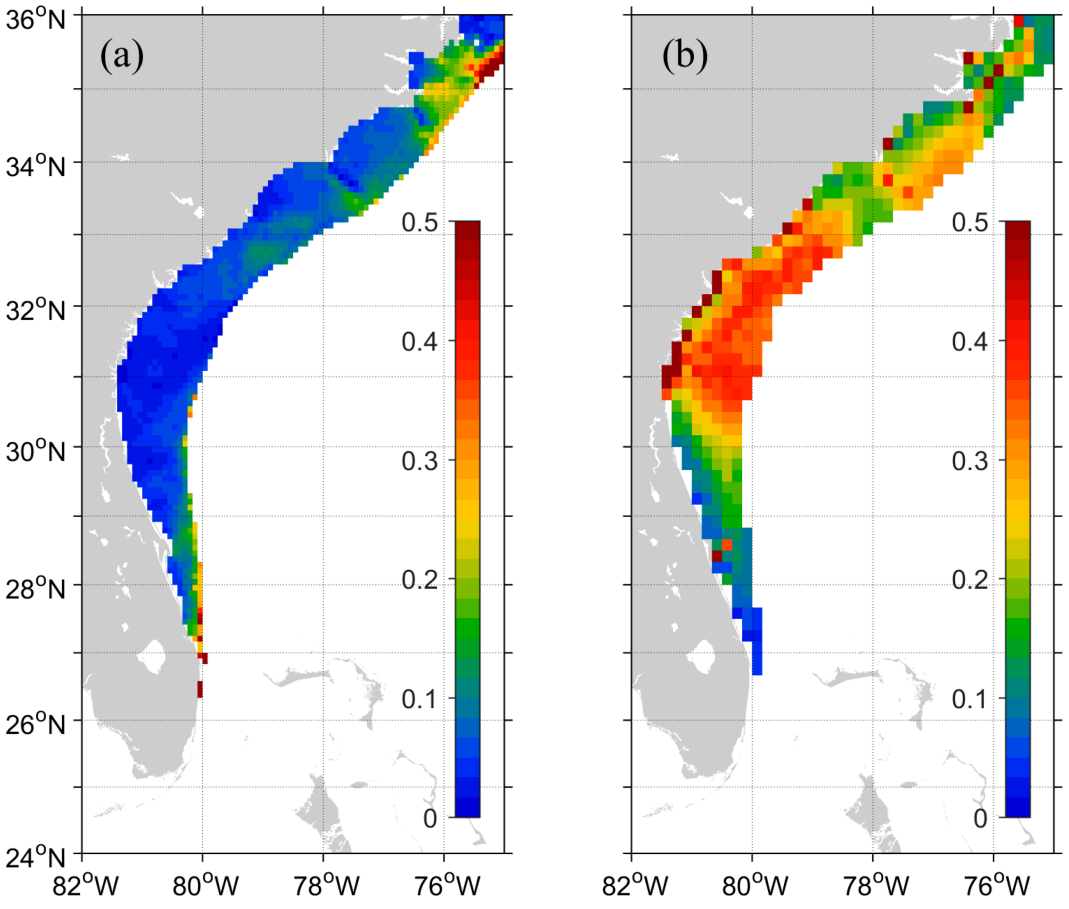

FIG. 3. (a) Time-averaged velocity magnitude (m s^{-1}) at the bottom and (b) the amplitude of M_2 tidal currents (m s^{-1}) on the continental shelf (water depth less than 500 m).

smoothed version of the open-ocean signals with an equatorward displacement and an attenuated magnitude; notably, the degree of displacement and attenuation is spatially uniform. Under the influence of tides (Fig. 5b), sea level on the shelf experiences less equatorward displacement and attenuation south of about 31°N (Fig. 5b). This is due to the abrupt increase of BFC between 28° and 35°N. Experiments show that this feature of smaller displacement and attenuation is insensitive to other model parameters, for example, the shelf slope or cross-shore width (figures not shown).

The second metric to evaluate the tidal impact is to examine the coastal sea level response to different spatial scales of open-ocean signals. Here, we only focus on signals of alongshore scales larger than 500 km, which exceed 2.5 times the shelf width of 200 km; namely, we do not examine signals with an alongshore scale comparable to the shelf width (Wu 2023). Results show that without tidal influence (Fig. 6a), oceanic signals with longer wavelengths would induce a stronger coastal response because of the larger decay distance. In contrast, short-wavelength variability of open-ocean sea level (500 km < wavelength < 2000 km) would be significantly suppressed when penetrating across the continental shelf and slope (Zhai et al. 2010; Lin et al. 2022). With tides included (Fig. 6b), a noticeable enhancement of signal transmission can be clearly seen south of 31°N, and the averaged increment of penetration rate reaches about 16% for all wavelengths. Notably, tidal effects are more pronounced for shorter-wavelength signals (500–1500 km), with transmission enhancements exceeding 20%.

To verify whether tide-induced enhancement of signal penetration is indeed more pronounced for shorter-wavelength signals (500 km < wavelengths < 1500 km), a series of experiments are conducted by varying the slope of the continental shelf. The maximum increase in signal penetration is examined (Fig. 7). When the slope is gentle (slope $< 1.5 \times 10^{-3}$ or depth of the shelf break < 300 m), the enhancement of signal transmission is quite significant for wavelengths < 3000 km, with the increased rate ranging between 35% and 70%. When the slope becomes steeper ($>2.5 \times 10^{-3}$), the effect of nonuniform BFC is negligible, and the increased rate is inconspicuous (<20%) for the shorter-wavelength signals.

4. Observational evidence

The encouraging results from the modified β-plane ATW model solutions clearly demonstrate that tides can enhance

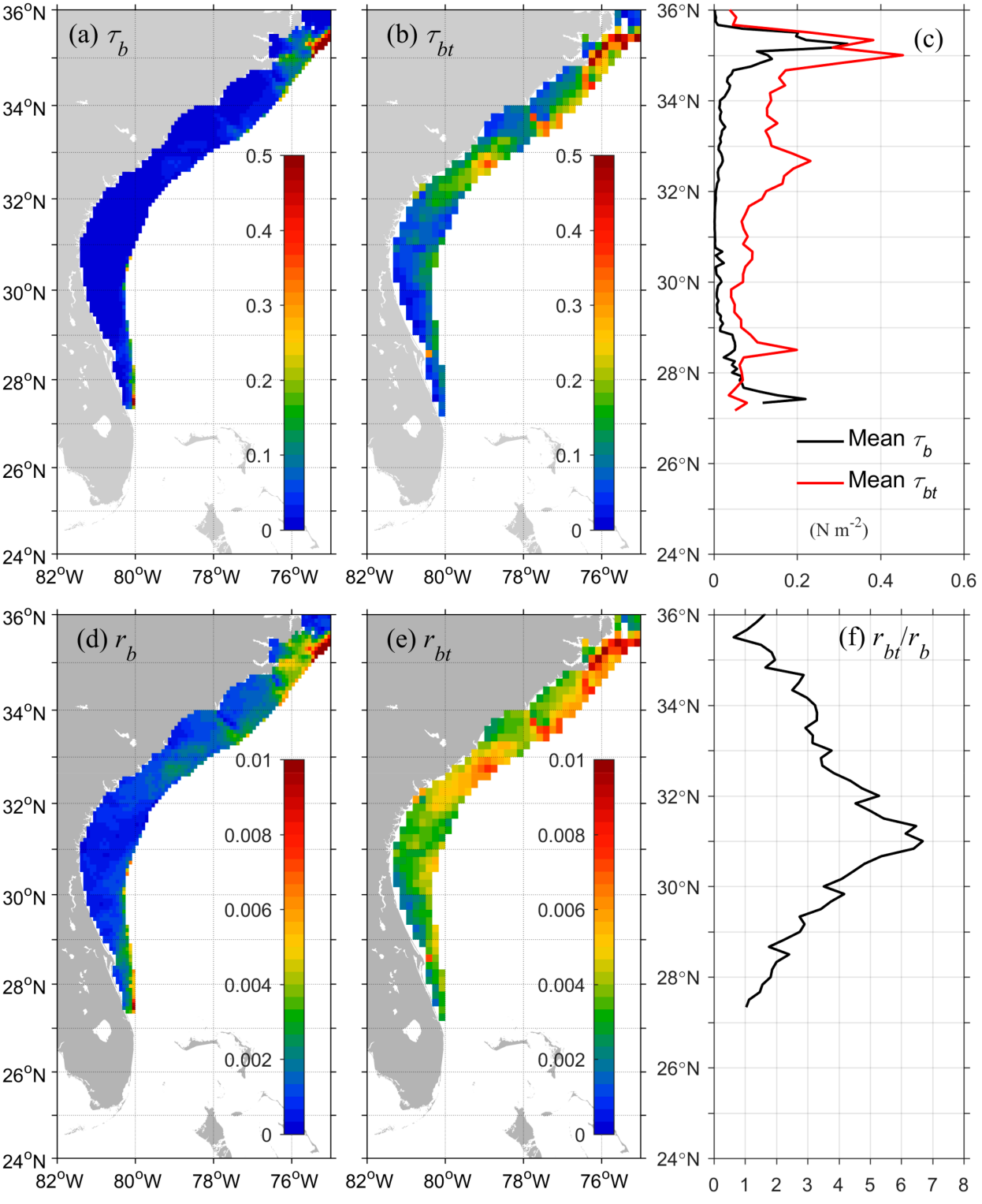

FIG. 4. BSS (N m^{-2}) caused by (a) mean currents (τ_b), (b) the combined mean and tidal currents (τ_{bt}), and (c) their zonal mean values. BFC (r; m s^{-1}) calculated from (d) τ_b and (e) τ_{bt}, as well as (f) the ratio of their zonal mean (r_{bt}/r_b).

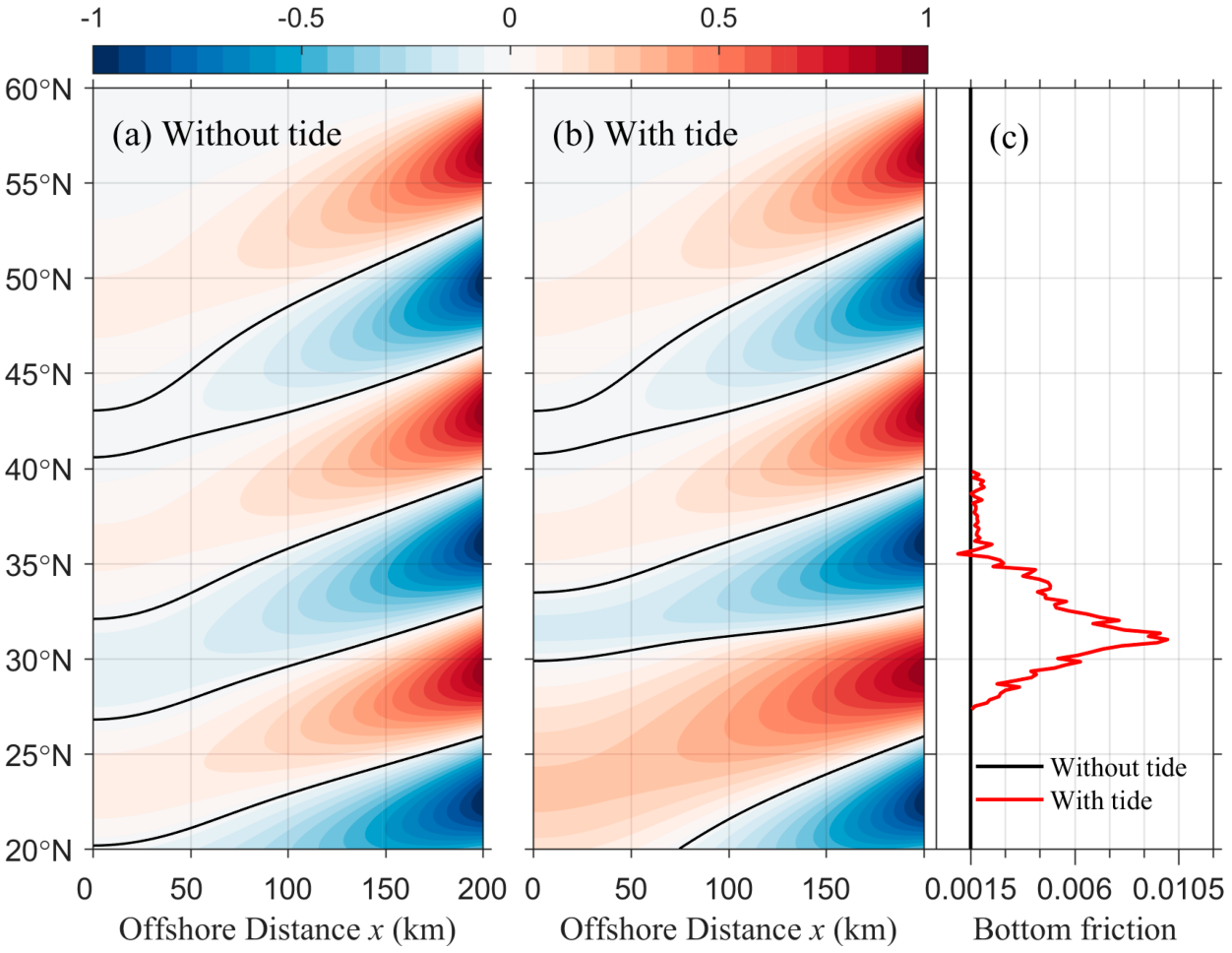

FIG. 5. Sea level distribution on the shelf (a) without tides and (b) with tides, using (c) different BFC profiles. The cross-shelf slope is 0.0025 (i.e., a depth change of 500 m over a 200-km-wide shelf). The alongshore wavelength of the open-ocean signal is 1500 km. The black lines in (a) and (b) denote zero contours. The sea level is normalized by the amplitude of open-ocean signals.

the shoreward penetration of offshore signals. In particular, the most pronounced coastal sea level response is found in the downstream vicinity of 31°N. It would be even more compelling to observe this tidal effect in the real ocean. Here, we attempt to verify the most salient feature of the tidal effect near 31°N using tide gauge observations along the east coast of North America (Fig. 8a).

First, we need to isolate the contribution of open-ocean signals from the observed sea level. The observed sea level anomalies from tide gauge measurements (η_{TG}), obtained from the revised local reference (RLR) dataset of the Permanent Service for Mean Sea Level (PSMSL) (Woodworth and Player 2003), are primarily affected by five dynamical factors: atmospheric pressure loads (i.e., inverted barometer effect; η_{IB}; Wunsch and Stammer 1997), steric height effect (η_{Steric}; Domingues et al. 2018; Volkov et al. 2019), alongshore wind stress (η_{Wind}; acts as forced coastal trapped waves; Lin et al. 2015, 2021), open-ocean forcing (η_{Open}; Wise et al. 2018; Dangendorf et al. 2021; Lin et al. 2022), and the sea level anomalies at a higher latitude (η_{CTW}) propagating equatorward via free coastal trapped waves (CTWs; Minobe et al. 2017). A simple equation is formulated as follows:

$$\eta_{TG} = \eta_{IB} + \eta_{Steric} + \eta_{Wind} + \eta_{CTW} + \eta_{Open}.$$

Compared with the signals from the ocean interior (η_{Open}), the other contributions (η_{IB}, η_{Steric}, η_{Wind}, and η_{CTW}) can be estimated more straightforwardly. Therefore, after removing the other components, the remnant will be used to represent η_{Open} (i.e., $\eta_{Open} = \eta_{TG} - \eta_{IB} - \eta_{Steric} - \eta_{Wind} - \eta_{CTW}$).

An inverse barometer adjustment is estimated by $\eta_{IB} = -(P - P_{ref})/\rho_0 g$, where ρ_0 is the seawater density, g is the gravitational acceleration, and a reference air pressure P_{ref} is equal to 1017.2 mb (1 hPa = 1 mb). The monthly surface pressure is obtained from the fifth generation ECMWF atmospheric reanalysis (ERA5). The steric height consists of thermosteric and halosteric components, which can be expressed as $\eta_{Steric} = \int_{-H}^{0} \alpha \Delta T dz + \int_{-H}^{0} \beta \Delta S dz$, where H is chosen to be 700 m considering the thermocline depth in this area; ΔT and ΔS are the temperature and salinity fluctuations relative to

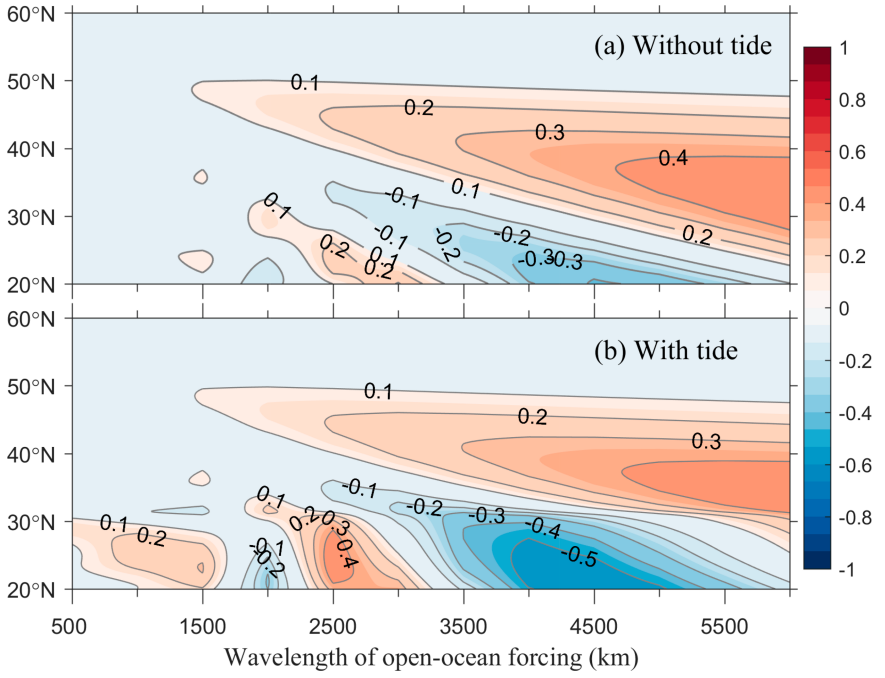

FIG. 6. Sea level at the coast as a function of the wavelength of open-ocean signals for the case (a) without tides and (b) with tides. The absolute values can be interpreted as the penetration rate of open-ocean signals since the coastal sea level has been normalized by the open-ocean sea level. The slope is fixed at 0.0025 in these experiments.

mean values over the study period at each layer, respectively; and α and β are the thermal expansion and salt contraction coefficients, respectively (Tabata et al. 1986). The steric height is calculated from the 3D hydrographic-gridded product EN4.2.2 generated by the Met Office Hadley Centre (Good et al. 2013). According to Csanady (1978), the alongshore wind-induced coastal sea level is determined by

$$\eta_{\mathrm{Wind}}(y) = \int_{y_0}^{y} -\frac{1.12fFs}{gr_{bt}}\{(-Ky)^{1/2} - [K(Y-y)]^{1/2}\}dy, \tag{23}$$

where g and f are the gravitational acceleration and the Coriolis parameter, respectively; alongshore wind stress F_s is prescribed for $Y > y > 0$; $K = r_{bt}/(fs)$, where s is the slope of the shelf; the integral route is along the coastline; and y_0 is the starting point of the integral route. Note that Eq. (23) incorporates the spatially varying bottom friction caused by tidal effects rather than using a constant drag coefficient, although the latter has been commonly employed in previous studies. This method has been extensively demonstrated to provide effective estimates of wind-induced coastal sea level variations (Hickey and Pola 1983; Nakanowatari and Ohshima 2014; Lin et al. 2021). The wind stress data are obtained from the ERA5, covering the period from 1950 to the present. After removing the three components (η_{IB}, η_{Steric}, and η_{Wind}) from the observed sea level, the residual contains contributions from both free CTW (η_{CTW}) and open-ocean signal penetration (η_{Open}). The spatially averaged residual reveals a coherent signal (not shown) that can be attributed to η_{CTW} since the rapid propagation of CTW generates long-distance coherent signals along the global continental slope (Hughes and Meredith 2006). Thus, we can isolate the open-ocean sea level contribution ($\eta_{\mathrm{OPEN}} = \eta_{\mathrm{TG}} - \eta_{\mathrm{IB}} - \eta_{\mathrm{Steric}} - \eta_{\mathrm{Wind}} - \eta_{\mathrm{CTW}}$) from the observed tide gauge measurements.

Here, we arbitrarily select the Springmaid Pier tide gauge station (Fig. 8a) as an example to display the time series of these sea level contributions and their summation (Fig. 8b). The results show that the amplitudes of the four components (η_{IB}, η_{Steric}, η_{Wind}, and η_{CTW}) are ~0.1 m, which is smaller than that of η_{TG} (~0.3 m). Their seasonal cycles are evident but not in phase with that of η_{TG}; however, their summation ($\eta_{\mathrm{IB}} + \eta_{\mathrm{Steric}} + \eta_{\mathrm{Wind}} + \eta_{\mathrm{CTW}}$) varies quite closely in both time and amplitude with the seasonal variations of η_{TG}. The residual between η_{TG} (black line) and $\eta_{\mathrm{IB}} + \eta_{\mathrm{Steric}} + \eta_{\mathrm{Wind}} + \eta_{\mathrm{CTW}}$ (red line) would be contributed by the open-ocean signals (η_{Open}).

Following the above procedures, we can similarly calculate time series of η_{Open} at other tide gauge stations (Fig. 9a). It is very interesting to observe that the temporal fluctuation magnitude of sea levels south of ~31°N is significantly larger than that north of 31°N, and it also exhibits notable multiyear variability. This finding suggests that the tide-induced enhanced penetration of open-ocean signals south of 31°N can indeed be detected in tide gauge measurements. However, three other factors may contribute to the abrupt change near ~31°N. First, a similar preexisted jump in the open-ocean sea level might propagate across the shelf/slope to the coast. Second, the potential influence of the closely nearshore Gulf

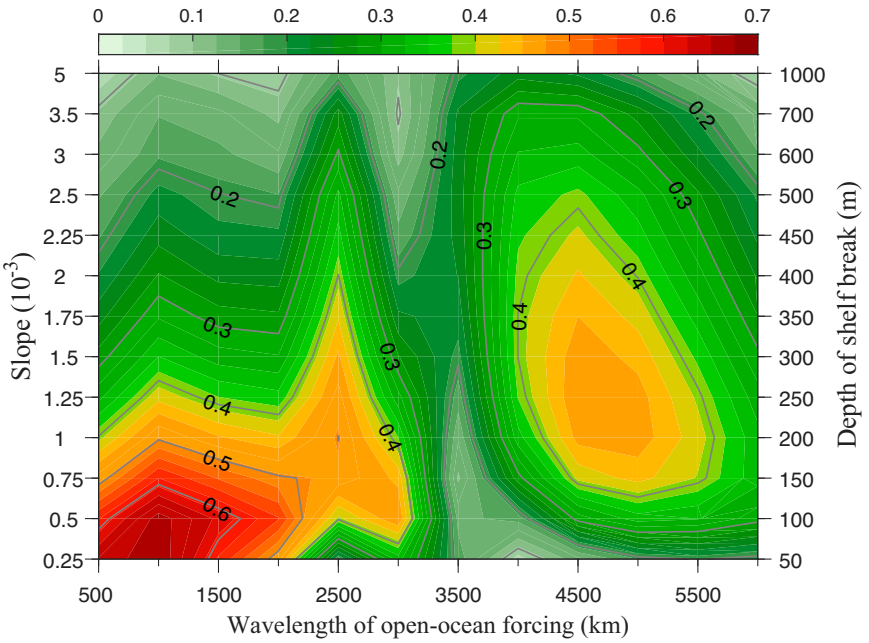

FIG. 7. The maximum enhancement of signal penetration as a function of shelf slope and the wavelength of open-ocean signals. The left axis is the slope of the continental shelf, and the right axis indicates the corresponding depth over a 200-km-wide shelf.

Stream. Third, the narrower shelf south of ~31°N. By calculating the oceanic barotropic and baroclinic responses to large-scale wind forcing in the North Atlantic basin and their transmission across the western boundary current (Minobe et al. 2017; Lin et al. 2022), we derive the alongshore profile of averaged sea level at the west wall of the Gulf Stream (η_W) (Fig. 9b). It is evident that η_W exhibits a nearly linear northward drop, consistent with prior studies (e.g., Higginson et al. 2015), but no abrupt change is observed north of 31°N. Therefore, the apparent coastal response near ~31°N is unlikely caused by the preexisting sea level jump in open-ocean signals. Figure 9c displays the alongshore profiles of averaged η_{IB}, η_{Steric}, and η_{Wind}, revealing that the alongshore tilt of η_{Steric} is markedly steeper than that of η_{IB} and η_{Wind}. In fact, the steric response (η_{Steric}) already incorporates the effect of Gulf Stream by accounting for thermal expansion or saline contraction of the water column (Kelly et al. 1999). Therefore, the influence of the nearby Gulf Stream on coastal sea level is embedded in the variations of η_{Steric} and thus cannot explain the abrupt changes in η_{Open} near 31°N either. Sensitivity tests (figures not shown) reveal that the enhancement induced by shelf width variations (<10%) is much weaker than that caused by the addition of tidal currents (50%). After eliminating these three potential factors, we conclude that the strong coastal response observed in tide gauge observations is mainly driven by tidal effects. This observed pattern of pronounced coastal response downstream vicinity of 31°N closely resembles the results of numerical simulations (Figs. 5b and 6b). The dramatic variations in observed sea level anomalies around 31°N not only confirm the reliability of our model results but, more importantly, validate the tidal effect in enhancing the shoreward propagation of open-ocean signals.

5. Conclusions and discussion

This study revisits the classic formulation of the β-plane ATW model, which is widely used to characterize open-ocean influences on coastal sea level. Previous interpretations of this model suggest that a larger bottom friction coefficient (BFC; r) enhances cross-shore diffusion and promotes the penetration of interior sea level signals to the coast. From the perspective of linear geostrophic vorticity balance, we obtain a new expression for the BFC, $r = f\delta_B$, which is no longer spatially uniform but instead varies with the Coriolis parameter f and the thickness of BBL δ_B. By adopting an eddy-viscosity parameterization ($A_v = \kappa u_* z$), we estimate the BBL thickness $\{\delta_B = \kappa[(\sqrt{\tau_b/\rho})/f]\}$ using known initial and enhanced bed shear stress τ_b. This approach yields a more realistic, spatially varying distribution of BFC $r = f\delta_B = \kappa\sqrt{\tau_b/\rho}$.

For a case study, in the western North Atlantic, our calculations demonstrate that incorporating tidal effects substantially increases both the total BSS and consequently BFC between 28° and 35°N relative to nontidal scenarios. The amplified BFC markedly strengthens the shoreward penetration of open-ocean signals at the corresponding latitudinal range, with tide gauge observations providing empirical support for this tide-enhanced transmission mechanism. Barotropic numerical simulations of coastal sea level response further reveal that this tidal enhancement exhibits wavelength dependence, showing greater amplification for shorter-wavelength open-ocean signals. Therefore, this new formulation, $r = f\delta_B = \kappa\sqrt{\tau_b/\rho}$, dynamically links high-frequency tidal processes with low-frequency open-ocean signal transmission, representing a significant advance in coastal dynamics by bridging traditionally separate time-scale phenomena.

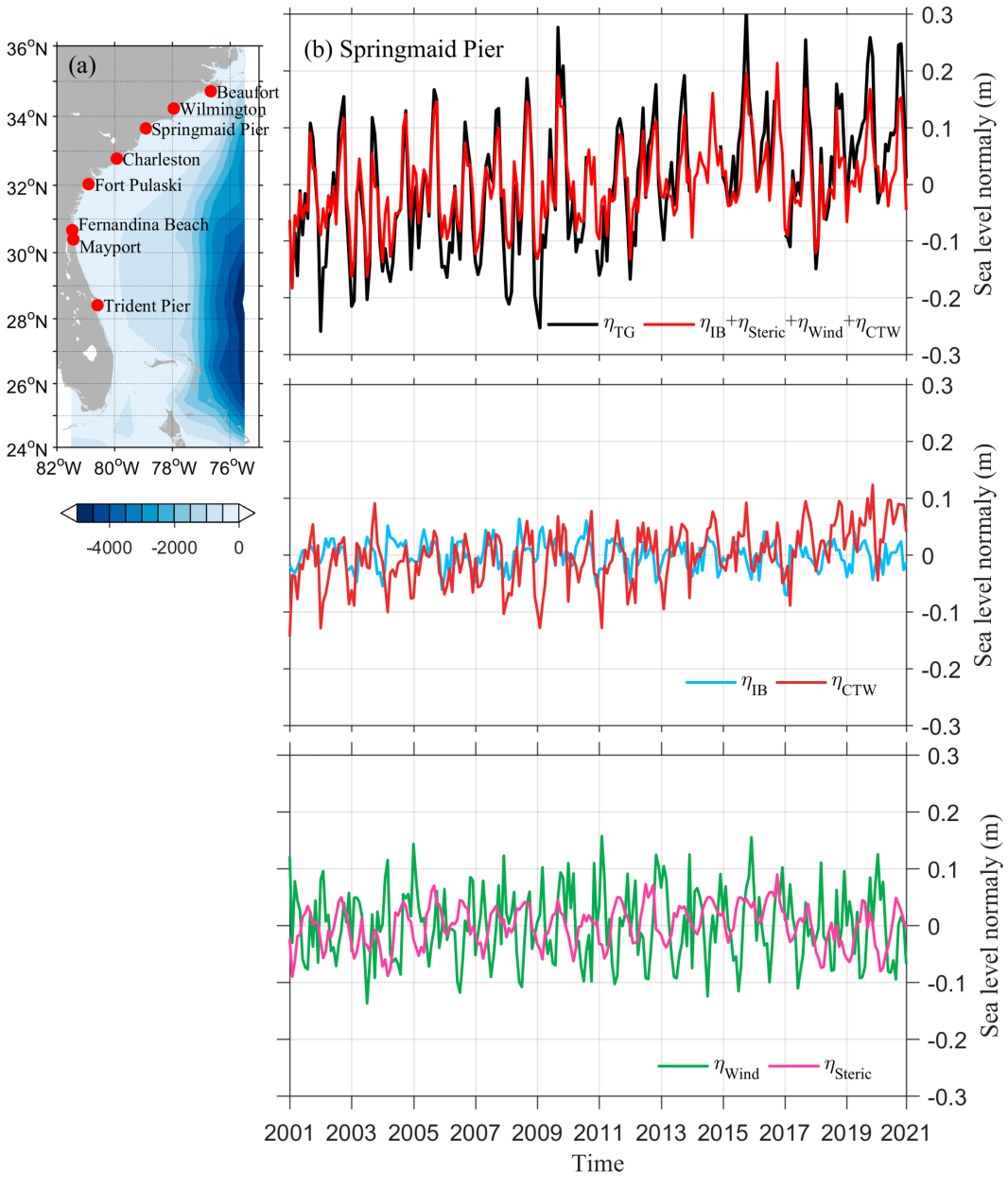

FIG. 8. (a) Locations of tide gauge stations along the east coast of North America. (b) Time series of observed sea level (η_{TG}; black line), and sea level contributions from the inverted barometer effect (η_{IB}; blue line), free CTW (η_{CTW}; dull-red line), alongshore wind stress (η_{Wind}; green line), steric height effect (η_{Steric}; pink line), and the sum of these contributions (red line) at Springmaid Pier tide gauge station.

This study primarily focuses on tide-induced modification of eddy viscosity (A_v), represented through a linear parameterization. In a simplified scenario where A_v is held constant, tidal effects can alternatively be parameterized via the tidal frequency σ. The σ is positive (negative) when tidal ellipses rotate counterclockwise (clockwise) in both hemispheres. Equation (11b) (i.e., $\delta_B = \sqrt{2A_v/f}$) reveals that δ_B can also be modulated by changes in the effective planetary frequency. Notably, tides with differing rotational directions on the shelf can indeed play a role in this regard; namely, the thickness of BBL considering the additional tides is then modified to $\delta_B = \sqrt{A_v/(|f+\sigma|)}$. In the absence of topographic constraints, tidal ellipses naturally rotate clockwise (counterclockwise) in the Northern (Southern) Hemisphere due to the Coriolis effect. This tidal rotation reduces the effective magnitude of planetary frequency, consequently increasing both δ_B and BFC. The key implication is that the presence of tides on the shelf generally enhances open-ocean signal penetration—a conclusion fully consistent with our core findings regarding tide-induced modification of A_v. Notably, numerical simulations

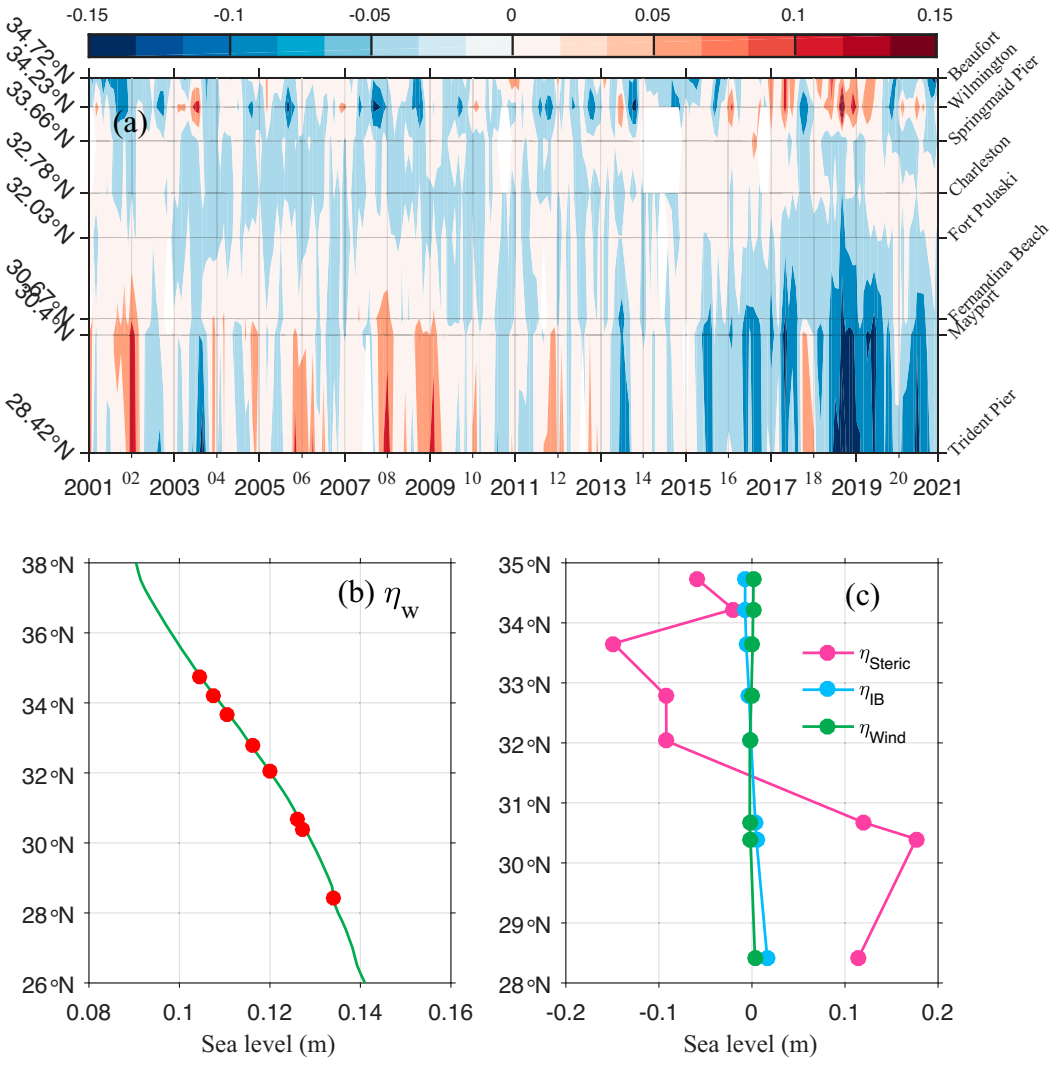

FIG. 9. (a) Time series of estimated open-ocean sea level signals (η_{Open}; m) at tide gauge stations along the east coast of North America (shown in Fig. 8a). (b) Alongshore profile of multiyear-averaged sea level at the west wall of the Gulf Stream (η_W; i.e., sea level in the open ocean). Red dots denote tide gauge locations. (c) Alongshore profiles of multiyear-averaged η_{IB}, η_{Steric}, and η_{Wind}.

employing the BFC formulation incorporating tidal frequency σ successfully reproduce the key characteristics of coastal response observed in tide gauge measurements along the east coast of North America (figures not shown).

In a broader context, the tidal effects emerge as nonnegligible and particularly critical when regional or global ocean models aim to simulate coastal responses to open-ocean dynamics. Our findings demonstrate that tide-excluded models systematically fail to accurately reproduce key characteristics of coastal response while significantly underestimating open-ocean signal penetration. While the barotropic simulations presented here provide a robust approximation for many shelf systems, future investigations should address the potential influence of stratification on these coastal responses. Such examination may further refine our understanding of tide-mediated cross-shelf transmission processes.

Acknowledgments. This study is supported by the National Natural Science Foundation of China (42306010, 42476009, 42076013) and the project funded by the China Postdoctoral Science Foundation (2023M742915). We are deeply grateful to the editor and the anonymous reviewers for their insightful comments and valuable suggestions, which significantly improved the quality of this manuscript. We also wish to express our sincere appreciation to Dr. Zhiyu Liu for the enlightening discussions during the revision process.

Data availability statement. Tide gauge sea level data are from the Permanent Service for Mean Sea Level (PSMSL; https://www.psmsl.org/). The ocean temperature and salinity data are from the Met Office Hadley Centre (https://www.metoffice.gov.uk/hadobs/en4/). Wind stress data and surface pressure are from the fifth generation ECMWF atmospheric

reanalysis (ERA5; https://www.ecmwf.int/en/forecasts/dataset/ecmwf-reanalysis-v5). The gridded monthly velocity data are obtained from CMEMS (https://data.marine.copernicus.eu/product/GLOBAL_MULTIYEAR_PHY_001_030). The tidal ellipse parameters are gained from the TPXO8 database (https://g.hyyb.org/archive/Tide/TPXO/TPXO_WEB/tpxo8_atlas.html).

REFERENCES

Baumert, H. Z., 2009: Primitive turbulence: Kinetics, Prandtl's mixing length, and von Karman's constant. arXiv, 0907.0223v2, https://doi.org/10.48550/arXiv.0907.0223.

Boumis, G., H. R. Moftakhari, and H. Moradkhani, 2023: Coevolution of extreme sea levels and sea-level rise under global warming. *Earth's Future*, **11**, e2023EF003649, https://doi.org/10.1029/2023EF003649.

Brink, K. H., 1991: Coastal-trapped waves and wind-driven currents over the continental shelf. *Annu. Rev. Fluid Mech.*, **23**, 389–412, https://doi.org/10.1146/annurev.fl.23.010191.002133.

——, 2006: Coastal-trapped waves with finite bottom friction. *Dyn. Atmos. Oceans*, **41**, 172–190, https://doi.org/10.1016/j.dynatmoce.2006.05.001.

Chapman, D. C., and K. H. Brink, 1987: Shelf and slope circulation induced by fluctuating offshore forcing. *J. Geophys. Res.*, **92**, 11 741–11 759, https://doi.org/10.1029/JC092iC11p11741.

Csanady, G. T., 1978: The arrested topographic wave. *J. Phys. Oceanogr.*, **8**, 47–62, https://doi.org/10.1175/1520-0485(1978)008<0047:TATW>2.0.CO;2.

Cushman-Roisin, B., 1994: Ekman layer. *Introduction to Geophysical Fluid Dynamics.* Prentice Hall, 219–248.

Dangendorf, S., T. Frederikse, L. Chafik, J. M. Klinck, T. Ezer, and B. D. Hamlington, 2021: Data-driven reconstruction reveals large-scale ocean circulation control on coastal sea level. *Nat. Climate Change*, **11**, 514–520, https://doi.org/10.1038/s41558-021-01046-1.

Domingues, R., G. Goni, M. Baringer, and D. Volkov, 2018: What caused the accelerated sea level changes along the U.S. East Coast during 2010–2015? *Geophys. Res. Lett.*, **45**, 13 367–13 376, https://doi.org/10.1029/2018GL081183.

Ellison, T. H., 1956: Atmospheric turbulence. *Surveys in Mechanics*, G. K. Batchelor and R. M. Davies, Eds., Cambridge University Press, 400–430.

Garrett, C., and E. Kunze, 2007: Internal tide generation in the deep ocean. *Annu. Rev. Fluid Mech.*, **39**, 57–87, https://doi.org/10.1146/annurev.fluid.39.050905.110227.

Good, S. A., M. J. Martin, and N. A. Rayner, 2013: EN4: Quality controlled ocean temperature and salinity profiles and monthly objective analyses with uncertainty estimates. *J. Geophys. Res. Oceans*, **118**, 6704–6716, https://doi.org/10.1002/2013JC009067.

Gross, T. F., and A. R. M. Nowell, 1985: Spectral scaling in a tidal boundary layer. *J. Phys. Oceanogr.*, **15**, 496–508, https://doi.org/10.1175/1520-0485(1985)015<0496:SSIATB>2.0.CO;2.

Hickey, B. M., and N. E. Pola, 1983: The seasonal alongshore pressure gradient on the West Coast of the United States. *J. Geophys. Res.*, **88**, 7623–7633, https://doi.org/10.1029/JC088iC12p07623.

Higginson, S., K. R. Thompson, P. L. Woodworth, and C. W. Hughes, 2015: The tilt of mean sea level along the east coast of North America. *Geophys. Res. Lett.*, **42**, 1471–1479, https://doi.org/10.1002/2015GL063186.

Hill, A. E., J. Brown, L. Fernand, J. Holt, K. J. Horsburgh, R. Proctor, R. Raine, and W. R. Turrell, 2008: Thermohaline circulation of shallow tidal seas. *Geophys. Res. Lett.*, **35**, L11605, https://doi.org/10.1029/2008GL033459.

Hughes, C. W., and M. P. Meredith, 2006: Coherent sea-level fluctuations along the global continental slope. *Philos. Trans. Roy. Soc.*, **A364**, 885–901, https://doi.org/10.1098/rsta.2006.1744.

——, I. Fukumori, S. M. Griffies, J. M. Huthnance, S. Minobe, P. Spence, K. R. Thompson, and A. Wise, 2019: Sea level and the role of coastal trapped waves in mediating the influence of the open ocean on the coast. *Surv. Geophys.*, **40**, 1467–1492, https://doi.org/10.1007/s10712-019-09535-x.

Hunter, J. R., 1975: A note on quadratic friction in the presence of tides. *Estuarine Coastal Mar. Sci.*, **3**, 473–475, https://doi.org/10.1016/0302-3524(75)90047-X.

Huthnance, J. M., 2001: Coastal trapped waves. *Encyclopedia of Ocean Sciences*, 2nd edn. J. H. Steele, Eds., Academic Press, 591–598.

——, 2004: Ocean-to-shelf signal transmission: A parameter study. *J. Geophys. Res.*, **109**, C12029, https://doi.org/10.1029/2004JC002358.

Ji, T., G. Li, and Y. Zhang, 2019: Observing storm surges in China's coastal areas by integrating multi-source satellite altimeters. *Estuarine Coastal Shelf Sci.*, **225**, 106224, https://doi.org/10.1016/j.ecss.2019.05.006.

Kelly, K. A., S. Singh, and R. X. Huang, 1999: Seasonal variations of sea surface height in the Gulf Stream region. *J. Phys. Oceanogr.*, **29**, 313–327, https://doi.org/10.1175/1520-0485(1999)029<0313:SVOSSH>2.0.CO;2.

Lee, H. J., K. T. Jung, M. G. G. Foreman, and J. Y. Chung, 2000: A three-dimensional mixed finite-difference Galerkin function model for the oceanic circulation in the Yellow Sea and the East China Sea. *Cont. Shelf Res.*, **20**, 863–895, https://doi.org/10.1016/S0278-4343(00)00005-4.

Lin, H., K. R. Thompson, J. Huang, and M. Véronneau, 2015: Tilt of mean sea level along the Pacific coasts of North America and Japan. *J. Geophys. Res. Oceans*, **120**, 6815–6828, https://doi.org/10.1002/2015JC010920.

Lin, W., H. Lin, and J. Hu, 2021: The tilt of mean dynamic topography and its seasonality along the coast of the Chinese mainland. *J. Geophys. Res. Oceans*, **126**, e2020JC016778, https://doi.org/10.1029/2020JC016778.

——, ——, ——, and L. Huang, 2022: Relative contributions of open-ocean forcing and local wind to sea level variability along the west coasts of ocean basins. *J. Geophys. Res. Oceans*, **127**, e2022JC019218, https://doi.org/10.1029/2022JC019218.

Luznik, L., R. Gurka, W. Zhu, W. A. M. Nimmo Smith, J. Katz, and T. R. Osborn, 2007: Distribution of energy spectra, Reynolds stresses, turbulence production, and dissipation in a tidally driven bottom boundary layer. *J. Phys. Oceanogr.*, **37**, 1527–1550, https://doi.org/10.1175/JPO3076.1.

Marshall, D. P., and H. L. Johnson, 2013: Propagation of meridional circulation anomalies along western and eastern boundaries. *J. Phys. Oceanogr.*, **43**, 2699–2717, https://doi.org/10.1175/JPO-D-13-0134.1.

Middleton, J. H., and R. E. Thompson, 1985: Steady wind-driven coastal circulation on a β-plane. *J. Phys. Oceanogr.*, **15**, 1809–1817, https://doi.org/10.1175/1520-0485(1985)015<1809:SWDCCO>2.0.CO;2.

Minobe, S., M. Terada, B. Qiu, and N. Schneider, 2017: Western boundary sea level: A theory, rule of thumb, and application

to climate models. *J. Phys. Oceanogr.*, **47**, 957–977, https://doi.org/10.1175/JPO-D-16-0144.1.

Nakanowatari, T., and K. I. Ohshima, 2014: Coherent sea level variation in and around the Sea of Okhotsk. *Prog. Oceanogr.*, **126**, 58–70, https://doi.org/10.1016/j.pocean.2014.05.009.

Pedlosky, J., 1987: Friction and viscous flow. *Geophysical Fluid Dynamics*, 2nd ed. Springer, 185–194.

Perlin, A., J. N. Moum, J. M. Klymak, M. D. Levine, T. Boyd, and P. M. Kosro, 2007: Organization of stratification, turbulence, and veering in bottom Ekman layers. *J. Geophys. Res.*, **112**, C05S90, https://doi.org/10.1029/2004JC002641.

Prandle, D., 1982: The vertical structure of tidal currents and other oscillatory flows. *Cont. Shelf Res.*, **1**, 191–207, https://doi.org/10.1016/0278-4343(82)90004-8.

Qiu, B., 2002: Large-scale variability in the midlatitude subtropical and subpolar North Pacific Ocean: Observations and causes. *J. Phys. Oceanogr.*, **32**, 353–375, https://doi.org/10.1175/1520-0485(2002)032<0353:LSVITM>2.0.CO;2.

——, 2003: Kuroshio Extension variability and forcing of the Pacific decadal oscillations: Responses and potential feedback. *J. Phys. Oceanogr.*, **33**, 2465–2482, https://doi.org/10.1175/2459.1.

Saylor, J. H., 1994: Studies of bottom Ekman layer processes and mid-lake upwelling in the Laurentian Great Lakes. *Water Quality. Res. J.*, **29**, 233–246, https://doi.org/10.2166/wqrj.1994.016.

Schlichting, H., and K. Gersten, 2016: *Boundary-Layer Theory.* Springer, 805 pp.

Simpson, J. H., and J. R. Hunter, 1974: Fronts in the Irish Sea. *Nature*, **250**, 404–406, https://doi.org/10.1038/250404a0.

——, J. Brown, J. Matthews, and G. Allen, 1990: Tidal straining, density currents, and stirring in the control of estuarine stratification. *Estuaries*, **13**, 125–132, https://doi.org/10.2307/1351581.

Soulsby, R. L., 1983: The bottom boundary layer of shelf seas. *Physical Oceanography of Coastal and Shelf Seas*, B. Johns, Elsevier, 189–266, https://doi.org/10.1016/S0422-9894(08)70503-8.

——, 1997: *Dynamics of Marine Sands: A Manual for Practical Applications.* Emerald Publishing Limited, 249 pp.

Stommel, H., 1948: The westward intensification of wind-driven ocean currents. *Eos, Trans. Amer. Geophys. Union*, **29**, 202–206, https://doi.org/10.1029/TR029i002p00202.

Suanda, S. H., F. Feddersen, and N. Kumar, 2017: The effect of barotropic and baroclinic tides on coastal stratification and mixing. *J. Geophys. Res. Oceans*, **122**, 10 156–10 173, https://doi.org/10.1002/2017JC013379.

Tabata, S., B. Thomas, and D. Ramsden, 1986: Annual and interannual variability of steric sea level along Line P in the northeast Pacific Ocean. *J. Phys. Oceanogr.*, **16**, 1378–1398, https://doi.org/10.1175/1520-0485(1986)016<1378:AAIVOS>2.0.CO;2.

Vallis, G. K., 2017: *Atmospheric and Oceanic Fluid Dynamics.* Cambridge University Press, 946 pp.

Volkov, D. L., S.-K. Lee, R. Domingues, H. Zhang, and M. Goes, 2019: Interannual sea level variability along the southeastern seaboard of the United States in relation to the gyre-scale heat divergence in the North Atlantic. *Geophys. Res. Lett.*, **46**, 7481–7490, https://doi.org/10.1029/2019GL083596.

Wise, A., C. W. Hughes, and J. A. Polton, 2018: Bathymetric influence on the coastal sea level response to ocean gyres at western boundaries. *J. Phys. Oceanogr.*, **48**, 2949–2964, https://doi.org/10.1175/JPO-D-18-0007.1.

Woodworth, P. L., and R. Player, 2003: The permanent service for mean sea level: An update to the 21st century. *J. Coastal Res.*, **19**, 287–295.

Wu, H., 2021: Beta-plane arrested topographic wave as a linkage of open ocean forcing and mean shelf circulation. *J. Phys. Oceanogr.*, **51**, 879–893, https://doi.org/10.1175/JPO-D-20-0195.1.

——, 2023: Incidence and reflection of offshore subinertial and barotropic pressure signals in wide shelf seas. *J. Phys. Oceanogr.*, **53**, 1691–1710, https://doi.org/10.1175/JPO-D-22-0234.1.

Wunsch, C., and D. Stammer, 1997: Atmospheric loading and the oceanic "inverted barometer" effect. *Rev. Geophys.*, **35**, 79–107, https://doi.org/10.1029/96RG03037.

Zhai, X., H. L. Johnson, and D. P. Marshall, 2010: Significant sink of ocean-eddy energy near western boundaries. *Nat. Geosci.*, **3**, 608–612, https://doi.org/10.1038/ngeo943.